J. Min. Metall. Sect. B-Metall. 58 (2) (2022) 285 - 297

Journal of Mining and Metallurgy, Section B: Metallurgy

THE EFFECT OF THE AMOUNT OF Y_2O_3 DOPED TO THE MA6000 ALLOY PRODUCED BY MECHANICAL ALLOYING METHOD ON WEAR BEHAVIOR

Ş. Çelik, D. Özyürek*, T. Tunçay

Karabuk University, Faculty of Technology, Department of Manufacturing Engineering, Karabuk, Turkey

(Received 13 January 2022; Accepted 16 June 2022)

Abstract

This paper investigated the wear performances of Y_2O_3 doped MA6000 (Ni-Cr-Al) alloy produced by mechanical alloying (MA). Produced, all powders were pre-formed by cold pressing and sintered in a vacuum environment. Sintered MA6000-X% Y_2O_3 superalloys were characterized by scanning electron microscopy (SEM), energy-dispersive spectroscopy (EDS), X-ray diffraction (XRD) analysis, density, and hardness measurements. Wear tests of Y_2O_3 added MA6000 alloys were carried out in a block-on-ring type wear device. In the wear tests, the sliding speed of 1 ms^{-1} at room temperature (RT) was performed under five different sliding distances (200-1000 m) and three different loads (5 N, 10 N, and 15 N). As a result of the studies, it was determined that the MA-ed MA6000 superalloy powders were homogeneous and flake shape. With the increase amount of Y_2O_3, hardness of these superalloys increased from 267 to 431 Hv, but the density slightly decreased. Different intermetallic/carbur phases such as Ni_3Al and MoC were observed in all compositions. Wear tests show that weight loss and wear rate decreased, and friction coefficient (μ) increased with the increasing amount of Y_2O_3 additive. Besides, it was determined that as the applied load increased in the wear test, the weight loss increased, but the wear rate and friction coefficient (μ) decreased.

Keywords: *Mechanical alloy; Superalloy; MA6000; Wear; Y_2O_3*

1. Introduction

With the use of superalloys in jet engines, the interest in these materials is increasing day by day. In order to meet the increasing energy demands and extend the life of jet engines, studies on the development of these materials continue [1,2]. Most of the superalloys used in jet engines are nickel-based and have traditionally been strengthened by precipitation of the γ′ phase in the polycrystalline face centered cubic (FCC) structured γ matrix phase [3]. Later, these alloys were used in many fields such as spacecraft, electricity generation, metallurgy, etc. [4].

Mechanical alloying (MA) is an effective method for producing oxide dispersion strengthened (ODS) alloys [5]. ODS Ni-based superalloys are widely used in industrial gas turbines and spacecraft [6–8]. In producing ODS Ni-based superalloys, oxide particles such as Y_2O_3, Al_2O_3, and ThO_2 are added to the nickel matrix [4]. In these alloys, the MA method provides both strengthening by γ′ phase precipitation and strengthening by dispersion of oxide particles [1]. One of the first and most important ODS alloys developed after discovering mechanical alloying (MA) is MA6000 [9]. When the MA6000 alloy is compared with conventional superalloys, it is understood that the small size (submicron) oxide particles homogeneously dispersed in the matrix play an essential role in developing high-temperature strength. In Ni-based oxide-dispersed superalloys, the thermal stability of the oxide particles distributed in the matrix at high temperatures is excellent. Oxide particles in the alloy structure prevent dislocation movement and increase high-temperature strength, creep, and fatigue strength (compared to superalloys produced by traditional methods such as casting) [10,11]. Kuz'min et al. [12] produced an Al-metal matrix composite with nano carbon (CNT) (in the range of 0.01 to 1.00 wt%) by powder metallurgy method, and they stated that the tensile test results were improved up to the addition of 0.1 wt.% CNT, then the CNT powders were agglomerated. In another study, Kuz'min et al. [13] found Al_4C_3 intermetallic in the microstructure investigations of nano carbon reinforced Al-metal matrix composites. They also emphasized that the electrical conductivity of the produced Al-CNT composite materials was very close to the cast material.

* *Corresponding author: dozyurek@karabuk.edu.tr*

https://doi.org/10.2298/JMMB220113010C

Some notable parts used in gas turbines are subjected to centrifugal forces, static and dynamic loads at high temperatures. As a result, wear and mass losses occur on the material surface [10,14]. In a study by Singer and Gessinger [9], it was stated that the MA6000 superalloy exhibited superplastic behavior under suitable hot working conditions. Although many studies have been carried out on MA6000 alloys, no study has been found on the alloy's microstructure and wear of the Y_2O_3 reinforcement phase.

Therefore, in this study, MA6000-X% Y_2O_3 alloys produced by the mechanical alloying method and added (doped) different amounts of Y_2O_3 (wt %) were produced. The produced MA6000-X% Y_2O_3 alloys were examined for microstructural and wear behavior.

2. Materials and Method

MA6000 superalloy used in the experimental study was produced from elemental Ni (99.9%) 44 µm, Cr (99%) 44 µm, Al (99%) (flake powder), W (99.9%) 10 µm, Ti (99.7%) 149 µm, Mo (99.9%) 1- 5 µm, Ta (99.9%) 44 µm, Zr (99%) 149 µm, C (99.95%) 2-12 µm, and B (99%) 2 µm powders. Elemental powders were obtained from Sigma Aldrich. The chemical composition of the MA6000 superalloy is given in Table 1.

Table 1. *The chemical composition of the MA6000 alloy used in the studies (wt %)*

Cr	Al	W	Ti	Mo	Ta	Zr	C	B	Ni
15	4.5	4	2.5	2	2	0.15	0.05	0.01	Bal.

Elemental powders were prepared in the quantities determined in Table 1 with a scale with a sensitivity of 1/10,000. The prepared powders were alloyed with 0.6, 1.2, 1.8, and 2.4% Y_2O_3 reinforcing phase in the planetary type mechanical alloying/milling (MA/MM) device of FRITSCH pulverisette company. 300 rpm stirring speed, 8 mm stainless steel ball (1:10 ratio), stearic acid (by weight) as process control chemical, and 300 minutes were used as mechanical alloying parameters. In order to prevent the heating of the powders placed in the milling jar, they were ground for 150 minutes and then left for 30 minutes. Elemental powders and high-energy balls were alloyed by the effect of centrifugal force and Coriolis force inside the container, which acted inversely to the direction of rotation. After MA/MM process, MA6000+X% Y_2O_3 powders were pressed uniaxially at room temperature with Ø12 steel mold under 700 MPa load. MA6000+X% Y_2O_3 green compacts were sintered at 1270°C for 120 minutes at a 4 °C /min heating rate under pressure (10-6 millibars) in a vacuum environment. Sintered MA6000+X% Y_2O_3 superalloys are prepared by metallographic processes according to ASTM E3 -11 standard, in 20ml HNO_3 and 80ml HCl solution for 120 seconds etched.

Density measurements of MA6000+X% Y_2O_3 superalloys (in Precisa brand density kit) were made according to Archimedes principle, and hardness measurements were made in Shimadzu brand microhardness device (under 490.3 mN load, 10 sec). Density and microhardness measurements were determined by taking the average density and microhardness values of 5 different samples. A scanning electron microscope (SEM + EDS) (in Carl Zeiss Ultra Plus Geminin (FEG) device) was used for microstructure investigations. The microstructure phases in MA6000+X% Y_2O_3 were characterized by X-Ray diffraction (XRD) (Rigaku Ultima IV -X-Ray Diffraction Spectrometer).

MA6000+X% Y_2O_3 alloys were tested on a nitride-hardened steel abrasive ring with a hardness of 68 HRC. Wear tests were carried out in a block-on-ring type standard test device according to the ASTM G77 standard. The worn surfaces of the produced MA6000+X% Y_2O_3 superalloys were washed with distilled water and methanol by applying standard metallographic procedures before the test. Wear tests were carried out at room temperature (RT) with a sliding speed of 1 ms^{-1} using five different sliding distances (200-1000m) and three different loads (5 N, 10 N, and 15 N). The weight loss, wear rate, and friction coefficient averages obtained from 3 different samples were calculated in the wear tests. The wear rate was calculated with the Equation 1

$$W_a = \frac{\Delta G}{d \cdot P \cdot S} \quad (1)$$

where Wa is the wear rate ($mm^3/N{\cdot}m$), ΔG is the weight loss (mg), d is the density (g/cm^3), P is the load (N), and S is the sliding distance (m). After the wear test, the wear surfaces of the samples were examined by SEM.

3. Results and Discussion

3.1. Characterization of MA6000/ Y_2O_3 powder particles

SEM images of the basic alloying element powders and the Y_2O_3 reinforcement phase are given in Figure 1 to study the dimensional and shape effect of the MA/MM process on elemental powders. It can be seen that the elemental Ni powder given in Figure 1.a had a polygonal structure and reticulate, and the powder size was less than 10 µm on average. Cr powders were seen in amorphous sharp-edged/angular shapes and different sizes (Figure 1. b). It is understood that the Al powders were flake-shaped and semi-smooth with sharp edges/angular; their thickness was relatively low (high surface

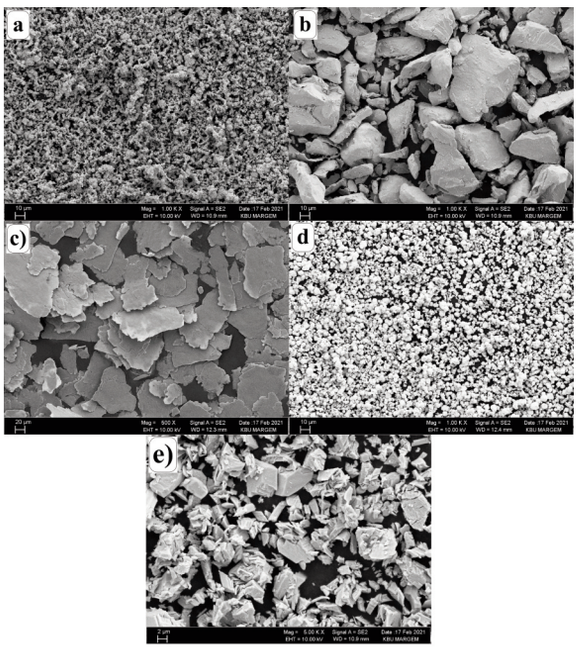

Figure 1. *The initial SEM images of the elemental powders used in the study were a) Ni, b) Cr, c) Al, d) W, and e) Y_2O_3*

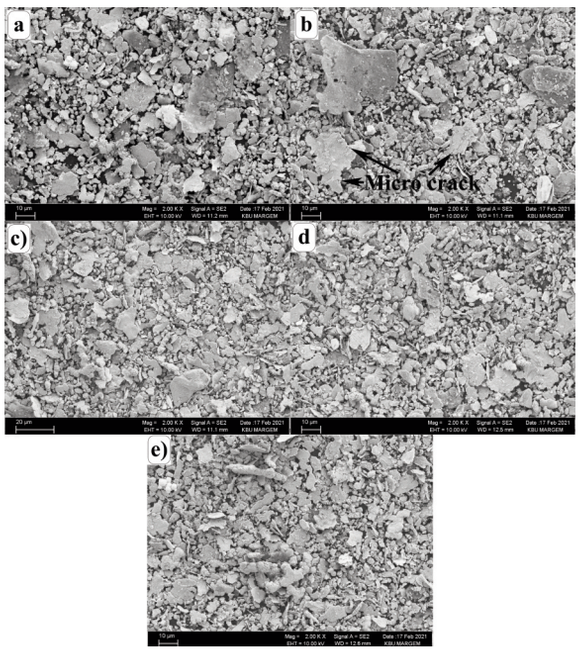

Figure 2. *SEM images of MA'ed powders; a) MA6000, b) MA6000 + 0.6% Y_2O_3, c) MA6000 + 1.2% Y_2O_3, d) MA6000 + 1.8% Y_2O_3 and e) MA6000 + 2.4% Y_2O_3*

area/thickness ratio) (Figure 1. c). W powders were spherical, and the powder size was less than 10 µm on average (Figure 1. d). On the other hand, Y_2O_3 powders were polygonal, sharp-edged/angular, with a powder size of less than 10 µm (Figure 1. e).

SEM images to determine the dimensional and shape changes of mechanically alloyed non-reinforced and X% Y_2O_3 reinforced MA6000 alloy powders are given in Figure 2. Elemental powders, initially reticulate, flake, and spherical, broke and shrank as they were subjected to repeated cold welding and deformation hardening during high-energy ball milling. The intense deformation effect and events such as cold welding, hardening, and fracture were related to the ductile or brittle character of the powder particles. Ductile powder particles such as Ni and Al became flake in the early stages of MA under high-energy ball impacts. As the deformation continued, the flake-shaped powder particles hardened. In the later stages of MA, these powders' particles broke down and became smaller [15–19].

Initially, polygonal and reticulate Ni powders (Fig. 1.a) and flake shaped Al powders (Fig. 1. c) appeared to be complex-shaped as they were subjected to intense deformation during the MA process (Fig. 2). When the initial powders given in Figure 1 were compared with the MA'ed powders given in Figure 2, it was seen that the flake-shaped powders (Figure 1c) were broken, and their surface areas decreased while their thicknesses increased. With the effect of deformation of ductile powders, micro-cracks were formed as shown in Figure 2.b; micro cracks grew and then broke with the continuation of the deformation. Kang et al [19] reported that due to severe deformation of the matrix phase, powder particles of various small sizes were formed alongside the large-surfaced powder particles. The main reason why the matrix material Ni took the form of flakes was its ductile character. In Figure 2, it can be seen that, in

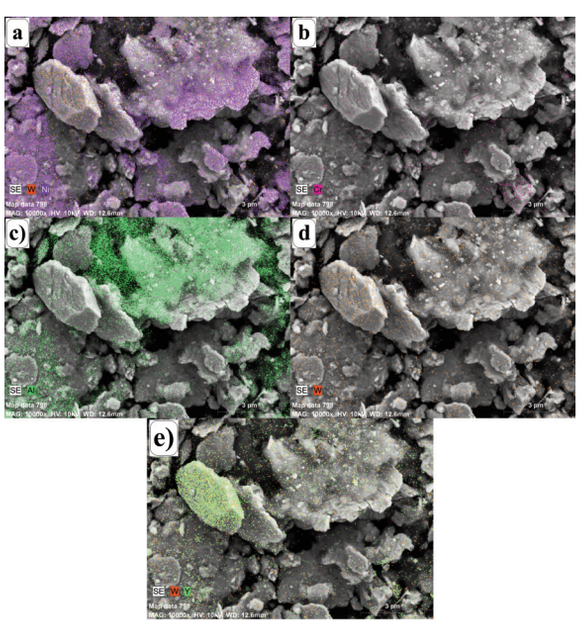

Figure 3. *SEM-Mapping images of mechanically alloyed MA6000+2.4% Y_2O_3 powders; a) Ni, b) Cr, c) Al, d) W, e) Y_2O_3*

general, powders with large surfaces turned into powders with smaller surfaces. This happened due to the hardness of the Y_2O_3 reinforcement phase.

EDS (Mapping) results of mechanically alloyed MA6000+2.4% Y_2O_3 powders are given in Figure 3. In Figure 3, it can be seen that Al powders (c) and Y_2O_3 powders (e) were evenly distributed except for one region, while the other powders exhibited an almost uniform distribution. After the addition of 2.4% wt. Y_2O_3 powder to the MA6000 alloy determined that the reinforcement phase agglomerated in some regions. A similar situation was observed in CNT added to the Al alloy [12,13].

3.2. Characterization of MA6000/X% Y_2O_3 Alloy Materials

SEM images of MA6000+X% Y_2O_3 superalloys after sintering are given in Figure 4, and EDS (point) results are given in Table 2. When the SEM images given in Figure 4 were examined, it was seen that there were porosities in the structure of all MA6000 superalloys produced. Some previous studies stated open and closed porosities in materials produced by powder metallurgy [2,5,20]. When the EDS results given in Table 2 were examined, it was understood that Ni-Ti-Cr intermetallic (1), Ni-rich Ti-Cr intermetallic (2), and Ta-rich Ni intermetallic (3) were formed in the structure (Figure 4.a). In the MA6000 superalloy (Figure 4. b) doped with 0.6% Y_2O_3, Ni-Cr intermetallic (1), Ta-rich Ni intermetallic (2), and a mottled grey, Ni-rich Al-C-Cr intermetallic (3) appeared. There were Ni-Ti intermetallic (1), C-Ni intermetallic/carbide (2), and Ni-Ti-Al intermetallic

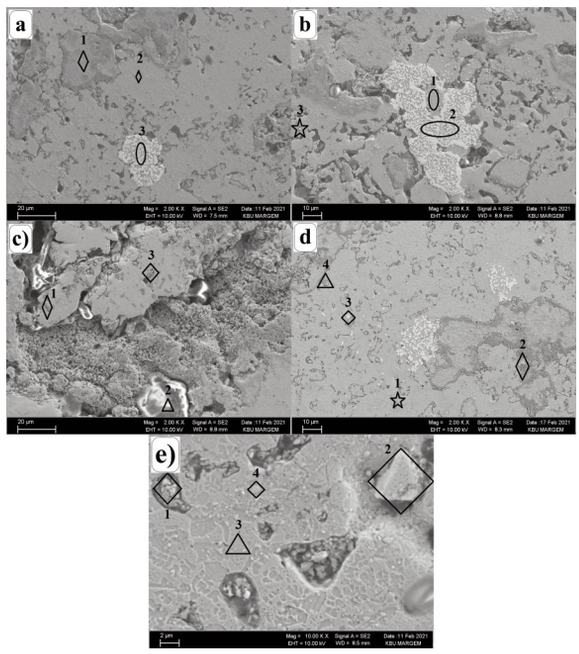

Figure 4. *SEM images of the microstructure of MA6000/X% Y_2O_3 superalloys a) MA6000, b) MA6000+0.6% Y_2O_3, c) MA6000+1.2% Y_2O_3, d) MA6000+1.8% Y_2O_3 and e) MA6000+2.4% Y_2O_3*

Table 2. *EDS analysis results of MA6000/X% Y_2O_3 alloys*

Alloys	Location	Elements (wt. %)										
		Ni	Cr	Al	W	Ti	Mo	Ta	Zr	C	O	Y
MA6000	1	36.7	10.13	1.84	1.17	28.2	1.04	2.3	-	8.19	10.42	-
	2	54.21	12.87	3.08	2.13	11.96	1.45	2.13	-	6.64	5.53	-
	3	18.59	6.07	2.13	-	1.33	-	59.62	-	6.79	5.47	-
MA6000 +0.6% Y_2O_3	1	55.45	14.69	3.84	1.66	0.79	1.76	10.07	0.08	4.71	5.99	0.98
	2	24.28	7.32	2.02	-	1.71	0.32	51.64	-	7.19	5.21	0.31
	3	37.81	10.73	14.9	1.91	0.36	0.59	1.72	-	12.8	19.02	0.15
MA6000 +1.2% Y_2O_3	1	39.95	9.36	5.17	1.39	17.72	0.12	0.21	0.13	5.43	20.35	0.16
	2	19.3	1.61	0.65	0.21	0.29	0.52	0.6	-	38.59	38.15	0.08
	3	17.57	8.39	12.88	0.35	13.14	-	6.02	-	6.1	31.98	3.55
MA6000 +1.8% Y_2O_3	1	64.26	11.64	5.52	1.96	1.1	1.3	3.91	-	3.11	5.23	1.97
	2	27.27	6.57	6.43	2.24	15.64	0.63	3.9	-	11.89	20.51	4.92
	3	35.09	8.97	8.04	1.2	3.02	1.16	9.05	-	5.39	16.82	11.28
	4	46.76	10.16	7.33	2.53	0.64	1.63	3.85	-	4.36	13.64	9.1
MA6000 +2.4% Y_2O_3	1	22.89	4.79	12.12	2.15	0.69	1.28	0.35	-	13.7	23.59	18.45
	2	1.3	1.29	0.44	5.53	-	-	-	-	6.04	17.79	67.59
	3	72.53	11.74	2.56	2.9	-	2.29	1.47	-	4.33	2.18	-
	4	9.11	0.52	6.46	4.28	-	2.42	-	-	5.07	22.99	49.15

(3) in the structure of MA6000 superalloy doped with 1.2% Y_2O_3 (Figure 4.c). Ni-rich Cr intermetallic/carbides (1) (Fig. 4.d), Ni-Ti-C intermetallic/carbide (2), Ni-Ta intermetallic (3), and Ni-Cr intermetallic (4) in MA6000 alloy with 1.8% Y_2O_3 doping were found. It was observed that Ni-Y intermetallic (1) Y-rich oxide compound (2,4) and Ni-rich Cr intermetallic (3) were formed in the 2.4% Y_2O_3 doped MA6000 alloy (Figure 4.e). Again, in Figure 4, in the SEM images of MA6000 and MA6000+X% Y_2O_3 doped superalloys, it was understood that the intermetallic formed in the structure were heterogeneously dispersed in different sizes and shapes in the matrix. It was seen that some of the small size intermetallic (<5 µm) were close to spherical; the rest were sharp-edged/angular. Some small-sized intermetallic appeared to come together to form large structures (50-60 µm) in complex shapes. Moreover, in Figure 4.a, it was seen that Ni_3Ti (1) had traces of Ni_3Al and Ni_3Ta intermetallic, and $Cr_{23}C_6$ and traces of MoC phases. In addition, it was understood that Ni_3Ti, Ni_3Al, Ni_3Ta intermetallic (2), and $Cr_{23}C_6$ and a small amount of MoC metal carbide phases were present. Furthermore, Ta-rich Ni_3Ta, trace amounts of Ni_3Al, Ni_3Ti intermetallic were formed in the 3rd region.

Likewise, when the regions in Figure 4. b-e were examined, it was seen that Ni_3Al, Ni_3Ti, Ni_3Ta intermetallic, and MoC and $Cr_{23}C_6$ metal carbides were present. Ezugwu et al. [21] reported that Ni_3Al, Ni_3Ti, Ni_3Ta (γ′) intermetallic phases in Ni-based superalloys used at high temperatures and heavy service conditions increased the strength of the alloy by precipitating in the matrix. Palavar et al. [22] in Ni-based superalloy studies, FCC γ′ $Ni_3(Al, Ti)$ intermetallic phase precipitated, Li et al. [23] and He et al. [24] reported that MC type carbides such as MoC were located at the grain boundaries in their studies. These carbides at the grain boundaries prevented grain boundary movement and growth at high temperatures. Thus, the strength of the superalloy also increased. In their study, Wu et al. [25] reported that $Cr_{23}C_6$ type carbides precipitated at the grain boundaries depending on the aging temperature and time by aging the Ni-based superalloy. Szczotok et al. [26] reported that MC type and $M_{23}C_6$ ($Cr_{23}C_6$) type carbides were formed at grain boundaries and between dendrites in their study to determine carbide structures in Ni-based superalloys.

Again, when the SEM images given in Figure 4. b, c, d, and e were examined, it was seen that Y_2O_3 was homogeneously distributed in the structure. When the Y_2O_3 reinforcement phase ratio was 2.4%, partial agglomeration was observed while the reinforcement phase was homogeneously dispersed in the matrix.

In Figure 5, XRD results obtained after sintering in MA6000/X% Y_2O_3 superalloys produced with MA

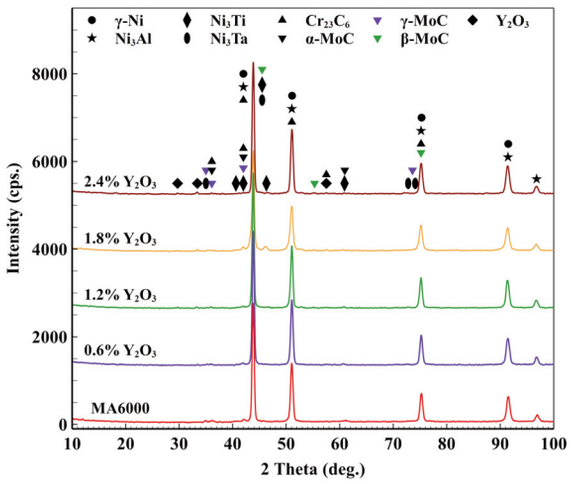

Figure 5. *XRD analysis results of MA6000/X% Y_2O_3 superalloys*

are given. When the XRD results given in Figure 5 were examined, it was determined that there was γ phase (Ni) (JCPDS 00-001-1260), Ni_3Al (JCPDS 03-065-0430), Ni_3Ti (JCPDS 00-002-1234), and Ni_3Ta (JCPDS 00-018-0893) intermetallic phases, $Cr_{23}C_6$ (JCPDS 00-014-0407) carbide phase ($M_{23}C_6$ type), Y_2O_3 (JCPDS 00-001-0831), and three different MoC (JCPDS 03-065-0280, JCPDS 03-065-3558 and JCPDS 00-006-0546) phases that made up the matrix in MA6000 superalloys in the structure. The morphology, size, and distribution of intermetallics such as γ′ (Ni_3Al, Ni_3Ti) and carbides such as MC and $M_{23}C_6$ were crucial for controlling the metallurgical and physical properties superalloys [27,28]. Al and Ti were added to superalloys to form γ′ (Ni_3Al, Ni_3Ti) intermetallic [22]. It is known that the γ′ (Ni_3Al, Ni_3Ti) intermetallic phase formed in the structure plays a significant role in the strengthening of superalloys and prevents the deterioration of the microstructure and mechanical properties of the alloy by preserving its chemical and physical properties up to temperatures close to the melting point (at temperatures above 600°C) [22,29–31].

Ni_3Ta (γ′) intermetallic phase had a strengthening effect in superalloys. It had a high melting temperature (1276.85°C) (1550 K). In a study by Kosorukova et al. [32,33], the orthorhombic, monoclinic and tetragonal Ni_3Ta intermetallic after annealing heat treatment at 699.85°C (973 K) was obtained.

MC, $M_{23}C_6$, M_6C, and M_7C_3 (rare) carbides were also important in controlling the properties of superalloys. MC type carbide structures provide strength to superalloys by preventing dislocation movement and grain boundary slippage at high temperatures. As hard MoC particles precipitated at the grain boundaries strengthen the grain boundaries (pinning), they increase the strength of the superalloy

by preventing grain growth and grain boundary slippage at temperatures around 1000 °C [23,24,27]. In this study, MC type carbide was quite scarce. This was because the amount of carbide-forming elements was low. Zhang et al. [27] reported that the low peak intensity occurred due to the low amount of MC carbides in the sintered alloys. Cheng et al. [34] stated that fcc was a crystalline MoC in their study. Liu et al. [35] stated three types of MoC in structure, α-MoC, β-MoC, and γ-MoC. $M_{23}C_6$ type carbides were formed in Ni-based superalloys with high Cr content in the 650-1100 °C. It precipitated at the grain boundaries in the temperature range of 704-871°C. Here M was mostly Cr [29,36]. This phase dissolved at 1125 °C [29].

Precipitated phases such as γ′ such as Ni_3Al, Ni_3Ti, Ni_3Ta, and γ″ such as Ni_3Nb and MC, $M_{23}C_6$, M_6C, and M_7C_3 carbides could maintain their structures up to temperatures close to melting/degradation degrees. When these intermetallic/carbide phases were exposed to high temperatures for a long time, they also deteriorated at temperatures below the melting/decay temperatures, reducing the superalloy's strength.

Y_2O_3 had high structural stability, strength and elastic modulus at high temperatures [37]. It had a high melting temperature of 2409.85 °C (2683 K). The cubic Y_2O_3 phase was more stable at high temperatures [38]. Due to these properties, Y_2O_3 was a suitable additive phase for strengthening superalloys. Y_2O_3 phase could maintain the strength of the superalloy for a long time at high temperatures by preventing dislocation movement.

In Figure 6, the experimental density, theoretical, and relative density results measured according to the Archimedes principle are shown. As seen in Figure 6, as the Y_2O_3 additive increased, the theoretical, experimental, and relative density decreased. This was because the density of Y_2O_3 was low (5.01 g/cm^3). Relative densities were 94.956%, 93.62%, 93.302%, 92.247%, 92.104% for MA600, MA6000+0.6% Y_2O_3, MA6000+1.2% Y_2O_3, MA6000+1.8% Y_2O_3, and MA6000+2.4% Y_2O_3 alloys, respectively. Depending on the increase in the amount of Y_2O_3 reinforcement phase added to the matrix, the amount of porosity in the structure increased. The harder Y_2O_3 reinforcement phase compared to Ni both increased the hardness of the matrix phase and prevented the dislocation motion. Therefore, the weight loss in the wear test of the produced MA6000 superalloys decreased, and the wear resistance improved [39].

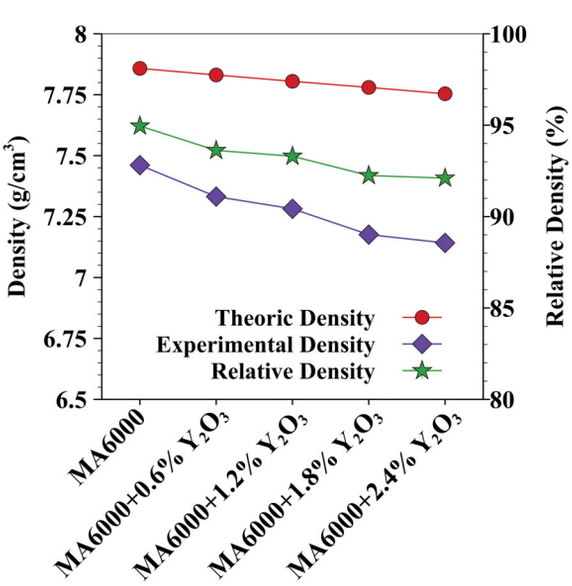

Figure 6. *Theoretical, experimental, and relative densities of MA6000 superalloys*

In Figure 7, the microhardness changes of superalloys are given. As the amount of Y_2O_3 additives increased, the microhardness increased. This was because the additive phase Y_2O_3 was a hard oxide that prevented grain boundary sliding.

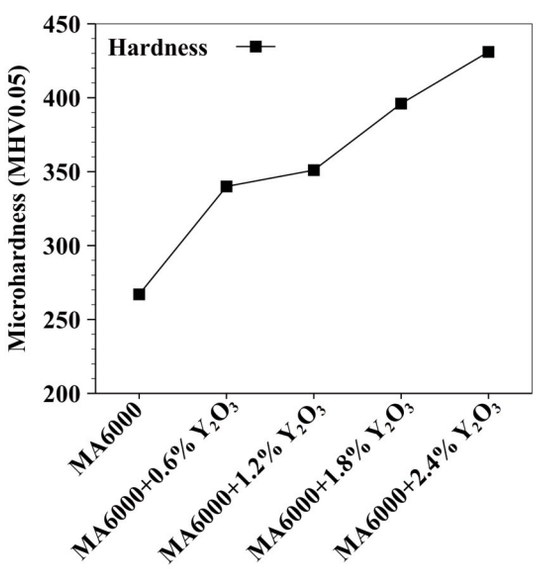

Figure 7. *Microhardness changes of MA6000 superalloys*

Mechanical properties such as hardness and strength were crucial factors for wear behavior. Therefore, these properties should be considered when examining the wear behavior of materials. In Figure 8 a, b and c, weight losses of MA6000 superalloys under different loads (5N, 10N, and 15N) are given. In MA6000 and MA6000+X% Y_2O_3 super alloys, weight losses increased as the sliding distance increased at all loads (5 N, 10 N, and 15 N). While the lowest weight loss was obtained under 5N load, the highest weight loss was obtained at 15 N. In the wear tests performed at 5 N, 10 N, and 15 N loads, the highest weight losses were observed in MA6000 and

MA6000+X% Y_2O_3 superalloys, while the lowest weight losses were in MA6000+2.4% Y_2O_3 superalloy. When the weight losses with 5 N, 10 N, 15 N loads and MA6000, MA6000+X% Y_2O_3 superalloys were compared, the lowest weight loss was obtained in MA6000+2.4% Y_2O_3 superalloy at 5 N load, while the highest weight loss was obtained in MA6000 superalloy at 15 N load. The reason for the highest weight loss (15 N) in the MA6000 superalloy was the high applied load and the low hardness of the alloy (267 Hv). The reason for the lowest weight loss (5 N) in the MA6000+2.4% Y_2O_3 alloy was the low applied load and the high hardness of the alloy (431 Hv). As the amount of hard Y_2O_3 additive phase increased, the weight losses of superalloys decreased. Y_2O_3 additive phase increased the wear resistance of superalloys.

Tian and Xu [40] coated the Ni plate surface with the nano sized Y_2O_3 phase (in the range of 1.56 to 4.40 wt.%) and reported an improvement in wear behavior. However, they did not give information about the wear resistance of the Ni matrix under the coating surface. Ikeno et al. [39] stated that the wear behavior of MA6000 alloy with 1% Y_2O_3 reinforcement and non-reinforced IN600, MAR-M427 alloys was higher than Ni. It was determined that the microhardness improved depending on the amount of Y_2O_3 reinforcement phase added to the MA 6000 alloy. This happened due to the interaction of both the reinforcement phase, the reinforcement phase, and the matrix phase. In XRD analysis (Fig. 5), it was determined that Ni_3Al, Ni_3Ti, and Ni_3Ta intermetallics were formed.

Palavar et al. [22] reported that the weight loss increased as the sliding distance increased in superalloys, and the lowest weight loss was obtained in the alloy with the highest hardness. On the other hand, Özyürek et al. [41] noted that with the increase of SiC reinforcement phase amount in MMCs, the wear weight loss decreased, and the wear resistance of MMCs was associated with an increase in hardness.

When the wear rate results of MA6000 and MA6000+X% Y_2O_3 doped superalloys, given in Figure 8 d, e and f, were examined, it was seen that while the sliding distance increased at 5 N, 10 N, and 15 N loads, the wear rates increased. In MA6000 and MA6000+X% Y_2O_3 superalloys, the highest wear rate was obtained in the samples applied with 5 N load, while the lowest wear rate was obtained in the samples applied with 15 N load. Qiao et al. [42] reported that the wear rate decreased as the applied load increased. The highest wear rate was recorded in MA6000 superalloy in all three loads, while the lowest was recorded in the MA6000+2.4% Y_2O_3 superalloy. The friction coefficient results obtained from the wear test of superalloys under three different loads (5 N, 10 N, and 15 N) are given in Figure 8 g, h and i.

The graph given in Figure 8 g, h and i shows that the friction coefficient (μ) of the alloys applied with three different loads (5 N, 10 N, and 15 N) exhibited a horizontal course. In the wear tests, the highest

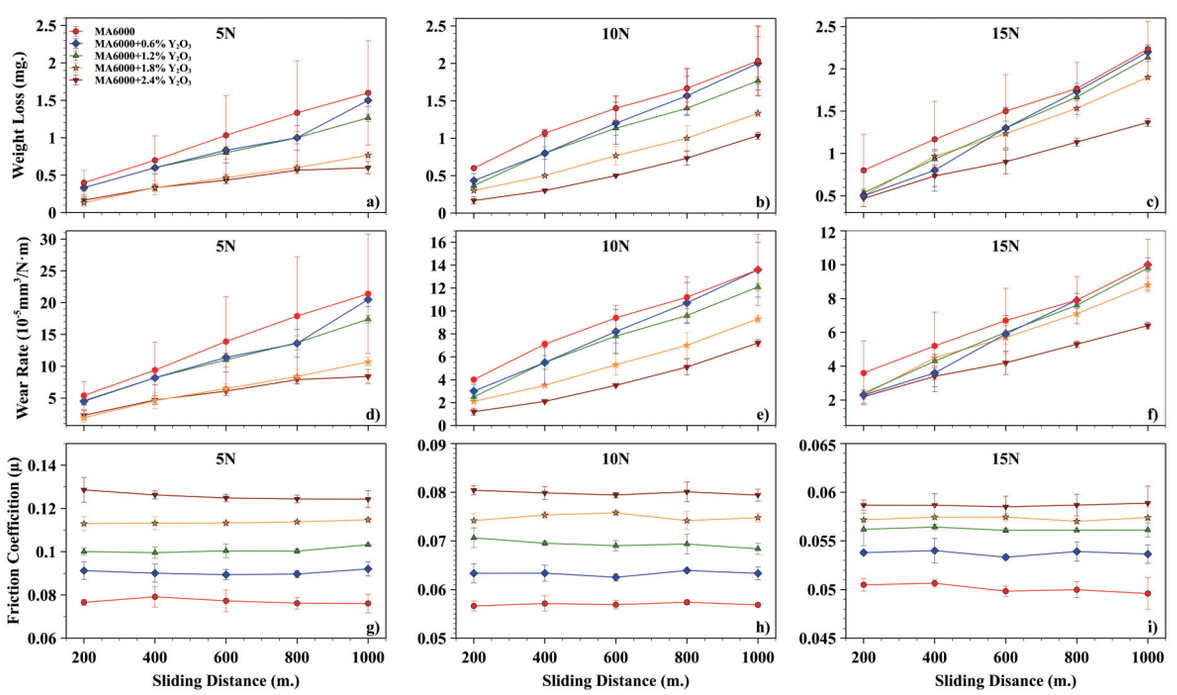

Figure 8. *The results of superalloys' weight loss, wear rate and friction coefficient obtained from the wear test under different loads (5N, 10N and 15N)*

friction coefficients were obtained in the samples applied with 5 N load in all compositions, while the lowest friction coefficients were obtained in the samples applied with 15 N load. At all loads, the lowest friction coefficients in MA6000 and MA6000+X% Y_2O_3 superalloys were obtained in samples applied with 15 N load, while the highest friction coefficients were obtained in samples applied with 5 N load. The friction coefficient (μ) decreased as the applied load increased in wear tests. The first reason for the decrease in the friction coefficient (μ) can be explained by the Equation 2.

$$\mu = \frac{F_s}{N} \tag{2}$$

where, Fs:Friction force (N); N:Normal Force(N); μ:Coefficient of Friction.

According to the Equation 2, it can be understood that the friction coefficient (μ) decreased when the applied load (N) increased (5 N, 10 N, and 15 N). The second reason was the heat increase in the contact surfaces with the increasing friction due to the increased applied load. Qiao et al. [42] reported that the friction coefficient decreased with the increasing of the applied load in the austenitic stainless steel wear test studies. The effect of the oxide layer formed on the surfaces by the effect of heat increase, making a solid lubricant effect. The friction coefficient depended on the friction surfaces. Since the Y_2O_3 additive phase was harder than the matrix phase, it created surface roughness during friction and caused an increase in the friction coefficient. In addition, increasing the Y_2O_3 additive phase increased delamination formation. The reason for the improvement in the wear resistance of the MA6000 alloy with the increase of the reinforcement phase was not only the reinforcement phase, but also the Ni_3Al, Ni_3Ti, and Ni_3Ta intermetallic phases determined in the structure.

Particles that broke off from the sample and the corresponding disk acted as the third element in the tribological system. These particles between the friction surfaces made friction difficult and caused the friction coefficient (μ) to increase. When the weight loss results given in Figure 8 a, b and c were compared with the friction coefficient results shown in Figure 8 g, h and i, it was understood that there was an inverse relationship between them. While the weight loss decreased in the abraded samples, the friction coefficient (μ) increased. According to the hardness results given in Figure 7, while the hardness of the alloys increased (the amount of Y_2O_3 additive phase increased), the friction coefficient (μ) increased. Thirugnanasambatham et al. [43] reported that the particles formed between the friction surfaces locked each other and prevented the sliding motion. Also, Panagopoulos et al. [44] reported that while the applied load on Ni-based superalloys increased, the debris between the rubbing surfaces increased, resulting in a decrease in the contact area and a decrease in the friction coefficient. Raghav et al. [45] added 2-8%wt. to Co-25C alloy. They alloyed with W by mechanical alloying method and stated that microhardness and compression strength were improved. They also noted that it was effective on wear resistance. Again Raghav et al. [46], in their other studies, synthesized Mg-Co (0-25Co) nanocomposites by powder metallurgy and noted that the microhardness, wear and corrosion resistance of Mg-25Co nanocomposite were better.

SEM images of MA6000 and X% Y_2O_3 superalloys after wear tests at room temperature, 1m/s shear rate, and under different loads (5 N, 10 N, and 15 N) are given in Figure 9. In Figure 9-a showed that the oxide film layer formed on the surface in the MA6000 superalloy after the wear under 5N load was broken by the effect of friction. It was understood that the region under the oxide layer was rough, and oxide particles of different shapes were scattered on the surface. In addition, there were micro cracks formed as a result of deformation on the surface. On the worn surfaces of 0.6% Y_2O_3 and 1.2%, Y_2O_3 reinforced MA6000 superalloys given in Figure 9' b and c, wear direction and traces, micro cracks, and particles detached from the surface could be seen. Micro-cracks perpendicular to the direction of friction form on the surface, which were deformed by the effect of the applied load. The formation of grooves in the sliding direction on the friction surface and the formation of microcracks perpendicular to the sliding direction indicated that the abrasive wear mechanism was active. According to Raghav et al. [46] and Banijamali et al. [47], various grooves and scratches formed parallel to the sliding direction and the wear test indicated the abrasive wear mechanism. In addition, they stated that fragile oxide areas were formed on the friction surfaces, and these oxide areas were disintegrated and dispersed on the surface as the friction continues. On the other hand, SEM image given in Figure 9-d (1.8% Y_2O_3 doped superalloy) showed fatigue wear. Micro cracks occurred due to plastic deformation caused by fatigue. As the wear continues, the microcracks caused the oxide particles to break off, and the oxide particles that broke off during the ongoing wear test became smaller by crumbling under the influence of the load. Raghav et al. [45] stated in their study that plastic deformation caused the formation of microcracks, and as a result, fatigue wear was dominant, and areas of debris were formed.

In the surface SEM image given in Figure 9-e (2.4% Y_2O_3 doped superalloy), it was seen that the oxide layer on the surface was at the beginning of the

fracture. Haji Ghassemi et al. [48] reported that cracks nucleated with plastic deformation on the surface during sliding in Al MMCs, the cracks caused delamination of oxide film and metallic particles.

In the SEM image of the worn surface given in Figure 9-f, the oxide layer, delamination area and deformed layer on the worn surface could be seen together. With the effect of friction, the oxide layer on the surface was broken and delamination areas were formed. In addition, the deformation layer, which was the lower layer, appeared when the debris moved away from the surface. In the SEM images of X%

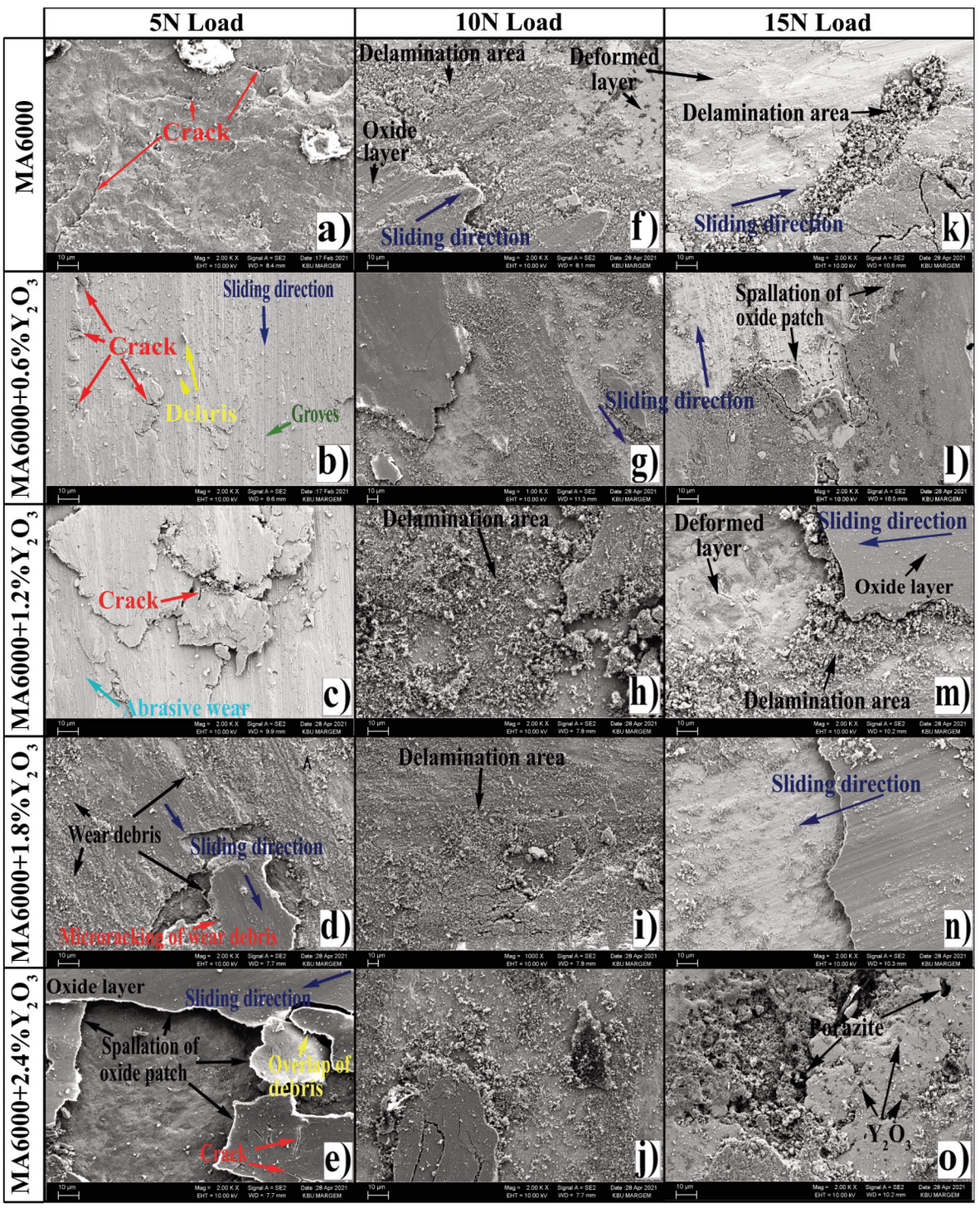

Figure 9. *Worn surface SEM images of MA6000, 0.6% Y_2O_3, 1.2% Y_2O_3, 1.8% Y_2O_3, and 2.4% Y_2O_3*

Y_2O_3 reinforced superalloys (Figure 9-g-h-i-j), oxide layer and delamination area were seen. From the SEM images of MA6000 and X% Y_2O_3 reinforced superalloys, it was understood that delamination type wear mechanism was dominant in the samples applied with 10 N load. Raghav et al. [49] reported that deleminations were effective in the wear of Al-Fe-SiC-Zr composites. Amanov [50] reported that an oxide and debris area formed between the rubbing surfaces. Thirugnanasambatham et al. [43], on the other hand, stated that a delamination type mechanism occurred in the early stages of wear, and a new lower layer emerged as a sliding surface after delamination. In another study by Lee et al. [51], it was stated that the deformation behavior of the lower layers of the friction surfaces was significant, and the dislocation density increased in this layer. The worn surface SEM image of the MA6000 superalloy shown in Figure 9-k showed the oxide layer, delamination area, and deformed layer on the wear surface. However, with increasing load, the delamination area decreased, and the deformation layer area increased. While the Y_2O_3 additive phase increased (Figure 9-l, m), the deformation layer area decreased. In the 2.4% Y_2O_3 reinforced superalloy (Figure 9-o), deformation layers and porosities were seen to remove the debris from the surface.

At the end of the 1000 m wear test, while the oxide layer on the surface of the MA6000 superalloy completely disappeared, the oxide layer on the wear surface of the 2.4% Y_2O_3 reinforced superalloy was just beginning to break. As a result of the wear test performed at 10 N load, a deformed layer was formed in the MA6000 superalloy, but this layer did not form with the increase in the amount of Y_2O_3 additive phase. Y_2O_3 additive had a positive effect on wear by delaying the breakage of the oxide layer formed on the wear surface of superalloys. This is in agreement with the weight loss graph given in Figure 8 a, b and c. In Figure 8 a, b and c, while the amount of Y_2O_3 additive phase increased, the wear weight loss decreased, and under 5 N load, the oxide layer breakdown was delayed. It can be seen from the SEM images given in e, j, and o (respectively) in Figure 9 that the oxide layer fracture on the superalloy wear surface increased with increasing applied load (5 N, 10 N, and 15 N). In addition, the weight loss results given in Figure 8 a, b and c also supported this situation. The weight loss increased as the applied load increased in wear tests, and the oxide layer breakage on the surface accelerated.

4. Conclusions

Within the scope of this study, MA6000, MA6000+X% Y_2O_3 powders were produced by the mechanical alloying method. The produced MA6000 and MA6000+X% Y_2O_3 superalloys were characterized, and their wear performances were investigated. The results obtained as a result of the studies are given below.

With the effect of mechanical alloying, the shape and size of the elemental powders changed, a nearly homogeneous distribution was exhibited in the structure, and the amount of Y_2O_3 additive phase increased, while the size of the alloy powders decreased.

The relative density ranged from 94.956% to 92.104%, depending on the amount of reinforcement phase. While the amount of the Y_2O_3 additive phase increased, the relative density decreased.

Microhardness varied between 267 Hv and 431 Hv depending on the amount of reinforcement phase. As the amount of the Y_2O_3 additive phase increased, microhardness increased.

From the results of XRD and SEM analysis, it was determined that γ-Ni matrix phase, Ni_3Al, Ni_3Ti and Ni3Ta intermetallic phases, MC and $M_{23}C_6$ type carbide phases (MoC, $Cr_{23}C_6$) were formed in the structure.

In the wear tests, the weight loss increased with the increase in the applied load and sliding distance, and the weight loss decreased with the increase in the amount of the Y_2O_3 additive phase.

The wear rate increased with the increase in the sliding distance, and the wear rate decreased with the increase in the load. In addition, as the amount of the Y_2O_3 additive phase increased, the wear rate decreased.

As a result of the wear tests, it was determined that the friction coefficient (μ) did not change with the sliding distance (it remained horizontal), and the friction coefficient (μ) decreased as the applied load increased. On the other hand, as the amount of the Y_2O_3 additive phase increased, the friction coefficient (μ) increased.

The SEM images after the wear test determined that the Y_2O_3 additive phase delayed the breakage of the oxide layer formed on the friction surface, and delamination zones were formed on the wear surface.

Author's Contributions

In this paper, each author has different contributions, such as organization, supply of consumables, laboratory work, and characterization. The authors' contributions are the following: Ş. Çelik performed laboratory studies such as MA/MM, and carried out wear tests; D. Özyürek managed the research process and supplied the necessary consumables, equipment; T. Tunçay analyzed SEM, XRD results.

Conflict of Interest Statement

We declare that all authors have no conflict of interest.

Data Availability Statement

The processed data needed to reproduce these findings cannot be shared at this time, as it also form part of an ongoing study.

References

[1] M. Mujahid, C.A. Gater, J.W. Martin, Microstructural study of a mechanically alloyed ODS superalloy, Journal of Materials Engineering and Performance, 7 (4) (1998) 524–532. https://doi.org/10.1361/105994998770347684.

[2] R.L. Dreshfield, Defects in nickel-base superalloys, Journal of Metals, 39 (7) (1987) 16–21. https://doi.org/10.1007/BF03258034.

[3] Y. Xu, L. Zhang, J. Li, X. Xiao, X. Cao, G. Jia, Z. Shen, Relationship between Ti/Al ratio and stress-rupture properties in nickel-based superalloy, Materials Science and Engineering A, 544 (2012) 48–53. https://doi.org/10.1016/j.msea.2012.03.006.

[4] D. Sun, C. Liang, J. Shang, J. Yin, Y. Song, W. Li, T. Liang, X. Zhang, Effect of Y 2 O 3 contents on oxidation resistance at 1150 °C and mechanical properties at room temperature of ODS Ni-20Cr-5Al alloy, Applied Surface Science, 385 (2016) 587–596. https://doi.org/10.1016/j.apsusc.2016.05.143.

[5] Y.L. Chen, A.R. Jones, Reduction of porosity in oxide dispersion-strengthened alloys produced by powder metallurgy, Metallurgical and Materials Transactions A: Physical Metallurgy and Materials Science, 32A (8) (2001) 2077–2085. https://doi.org/10.1007/s11661-001-0019-8.

[6] S. Ukai, K. Taya, K. Nakamura, M.S. Aghamiri, N. Oono, S. Hayashi, T. Okuda, Directional recrystallization by zone annealing in a Ni-based ODS superalloy, Journal of Alloys and Compounds, 744 (2018) 204–210. https://doi.org/10.1016/j.jallcom.2018.01.406.

[7] I. Baker, B. Iliescu, J. Li, H.J. Frost, Experiments and simulations of directionally annealed ODS MA 754, Materials Science and Engineering A, 492 (1-2) (2008) 353–363. https://doi.org/10.1016/j.msea.2008.03.032.

[8] A. Tomaszewska, Primary Microstructure Characterization of Co-20Ni-9Al-7W-3Re-2Ti Superalloy, Journal of Mining and Metallurgy, Section B: Metallurgy, 58 (1) (2022) 43–49. https://doi.org/10.2298/JMMB210309044T.

[9] J.K. Gregory, J.C. Gibeling, W.D. Nix, High temperature deformation of ultra-fine-grained oxide dispersion strengthened alloys, Metallurgical Transactions A, 16 (5) (1985) 777–787. https://doi.org/10.1007/BF02814828.

[10] M. Nganbe, M. Heilmaier, High temperature strength and failure of the Ni-base superalloy PM 3030, International Journal of Plasticity, 25 (5) (2009) 822–837. https://doi.org/10.1016/j.ijplas.2008.06.005.

[11] W. Hoffelner, R.F. Singer, High-cycle fatigue properties of the ODS-alloy MA 6000 at 850 °C, Metallurgical Transactions A, 16A (3) (1985) 393–399. https://doi.org/10.1007/BF02814337.

[12] M.P. Kuz'min, M.Yu. Kuz'mina, A.S. Kuz'mina, Production and properties of aluminum-based composites modified with carbon nanotubes, Materials Today: Proceedings, 19 (2019) 1826–1830. https://doi.org/10.1016/j.matpr.2019.07.021.

[13] M.P. Kuz'min, N.A. Ivanov, V. V. Kondrat'ev, V.G. Grigor'ev, M.Y. Kuz'mina, A.I. Begunov, A.S. Kuz'mina, N.N. Ivanchik, Preparation of Aluminum–Carbon Nanotubes Composite Material by Hot Pressing, Metallurgist, 61 (9-10) (2018) 815–821. https://doi.org/10.1007/s11015-018-0569-2.

[14] A. Korashy, H. Attia, V. Thomson, S. Oskooei, Characterization of fretting wear of cobalt-based superalloys at high temperature for aero-engine combustor components, Wear, 330–331 (2015) 327–337. https://doi.org/10.1016/j.wear.2014.11.027.

[15] C. Suryanarayana, Mechanical Alloying: A novel technique to synthesize advanced materials, Research Official Journal of Cast, 2019 (2019) 1–17. https://doi.org/10.34133/2019/4219812.

[16] R. Sundaresan, F.H. Froes, Mechanical alloying, Journal of Metals, 39 (8) (1987) 22–27. https://doi.org/10.1007/BF03258604.

[17] C.C. Koch, J.D. Whittenberger, Mechanical milling/alloying of intermetallics, Intermetallics, 4 (5) (1996) 339–355. https://doi.org/10.1016/0966-9795(96)00001-5.

[18] H.I. Gharsallah, A. Sekri, M. Azabou, L. Escoda, J.J. Suñol, M. Khitouni, Structural and thermal study of nanocrystalline Fe-Al-B slloy prepared by mechanical alloying, Metallurgical and Materials Transactions A: Physical Metallurgy and Materials Science, 46A (8) (2015) 3696–3704. https://doi.org/10.1007/s11661-015-2966-5.

[19] S.K. Kang, R.C. Benn, Characterization of INCONEL alloy MA 6000 powder, Metallurgical Transactions A, 18 (6) (1987) 747–752. https://doi.org/10.1007/BF02646916.

[20] C. Vincent, J.F. Silvain, J.M. Heintz, N. Chandra, Effect of porosity on the thermal conductivity of copper processed by powder metallurgy, Journal of Physics and Chemistry of Solids, 73 (3) (2012) 499–504. https://doi.org/10.1016/j.jpcs.2011.11.033.

[21] E.O. Ezugwu, J. Bonney, Y. Yamane, An overview of the machinability of aeroengine alloys, Journal of Materials Processing Technology, 134 (2) (2003) 233–253. https://doi.org/10.1016/S0924-0136(02)01042-7.

[22] O. Palavar, D. Özyürek, A. Kalyon, Artificial neural network prediction of aging effects on the wear behavior of IN706 superalloy, Materials and Design, 82 (2015) 164–172. https://doi.org/10.1016/j.matdes.2015.05.055.

[23] S. Li, Q. Wei, Y. Shi, C.K. Chua, Z. Zhu, D. Zhang, Microstructure characteristics of Inconel 625 superalloy manufactured by selective laser melting, Journal of Materials Science and Technology, 31 (9) (2015) 946–952. https://doi.org/10.1016/j.jmst.2014.09.020.

[24] Y.M. He, J.G. Yang, S.J. Chen, Z. Li, Z.L. Gao, Effect of high-temperature aging on microstructure and mechanical properties of Ni-Mo-Cr based superalloy subjected to simulated heat-affected zone thermal cycle, Journal of Alloys and Compounds, 660 (2016) 266–275.

https://doi.org/10.1016/j.jallcom.2015.11.129.

[25] Q. Wu, H. Song, R.W. Swindeman, J.P. Shingledecker, V.K. Vasudevan, Microstructure of long-term aged IN617 Ni-base superalloy, Metallurgical and Materials Transactions A: Physical Metallurgy and Materials Science, 39A (11) (2008) 2569–2585. https://doi.org/10.1007/s11661-008-9618-y.

[26] A. Szczotok, K. Rodak, Microstructural studies of carbides in MAR-M247 nickel-based superalloy, IOP Conference Series: Materials Science and Engineering, 35 (1) (2012) 1-11. https://doi.org/10.1088/1757-899X/35/1/012006.

[27] L. Zhang, X. Chen, D. Li, C. Chen, X. Qu, X. He, Z. Li, A comparative investigation on MIM418 superalloy fabricated using gas- and water-atomized powders, Powder Technology, 286 (2015) 798–806. https://doi.org/10.1016/j.powtec.2015.09.023.

[28] J. Belan, GCP and TCP Phases Presented in Nickel-base Superalloys, Materials Today: Proceedings, 3 (4) (2016) 936–941. https://doi.org/10.1016/j.matpr.2016.03.024.

[29] X. Wang, Y. Zhou, Z. Zhao, Z. Zhang, Effects of solutioning on the dissolution and coarsening of γ′ precipitates in a nickel-based superalloy, Journal of Materials Engineering and Performance, 24 (4) (2015) 1492–1504. https://doi.org/10.1007/s11665-014-1368-y.

[30] R. Frisk, N. A. I. Andersson, B. Rogberg, Cast structure in alloy A286, an iron-nickel based superalloy, Metals, 9 (6) (2019) 711. https://doi.org/10.3390/met9060711.

[31] Y. Nunomura, Y. Kaneno, H. Tsuda, T. Takasugi, Phase relation and microstructure in multi-phase intermetallic alloys based on Ni3Al-Ni3Ti-Ni3V pseudo-ternary alloy system, Intermetallics, 12 (4) (2004) 389–399. https://doi.org/10.1016/j.intermet.2003.12.011.

[32] T. Kosorukova, G. Firstov, H. NoËl, V. Ivanchenko, Crystal structure changes in the Ni3Ta intermetallic compound, Chemistry of Metals and Alloys, 6 (3/4) (2013) 196–199. https://doi.org/10.30970/cma6.0270.

[33] P. Li, J. Zhang, S. Ma, H. Jin, Y. Zhang, W. Zhang, First-principles investigations on structural, elastic, electronic properties and Debye temperature of orthorhombic Ni3Ta under pressure, Philosophical Magazine, 98 (18) (2018) 1641–1655. https://doi.org/10.1080/14786435.2018.1453619.

[34] L. Cheng, X. Yu, J. Zhang, W. Li, C. Zhao, Z. Wang, L. Jin, DFT investigations into surface stability and morphology of δ-MoC catalyst, Applied Surface Science, 497 (2019) 143790. https://doi.org/10.1016/j.apsusc.2019.143790.

[35] Y. Liu, Y. Jiang, J. Feng, R. Zhou, Elasticity, electronic properties and hardness of MoC investigated by first principles calculations, Physica B: Condensed Matter, 419 (2013) 45–50. https://doi.org/10.1016/j.physb.2013.03.016.

[36] K. Zhao, L.H. Lou, Y.H. Ma, Z.Q. Hu, Effect of minor niobium addition on microstructure of a nickel-base directionally solidified superalloy, Materials Science and Engineering A, 476 (1-2) (2008) 372–377. https://doi.org/10.1016/j.msea.2007.06.041.

[37] G. Zhu, S. Zhao, R. Wang, A. Dong, L. Zhang, W. Wu, W. Wang, S. Jiang, Y. Pu, Oxide reinforced Ni base composite prepared by spark plasma sintering, MATEC Web Conf. 130 (2017) 8–10. https://doi.org/10.1051/matecconf/201713003008.

[38] M. Hajizadeh-Oghaz, R.S. Razavi, M. Barekat, M. Naderi, S. Malekzadeh, M. Rezazadeh, Synthesis and characterization of Y2O3 nanoparticles by sol–gel process for transparent ceramics applications, Journal of Sol-Gel Science and Technology, 78 (3) (2016) 682–691. https://doi.org/10.1007/s10971-016-3986-3.

[39] S. Ikeno, I. Siota, M. Nobuki, M. Nakamura, Wear properties of oxide dispersion strengthened nickel alloys, Journal of Materials Science, 30 (17) (1995) 4401–4406. https://doi.org/10.1007/BF00361524.

[40] L. Tian, J. Xu, Electrodeposition and characterization of Ni-Y 2 O 3 composite, Applied Surface Science, 257 (17) (2011) 7615–7620. https://doi.org/10.1016/j.apsusc.2011.03.140.

[41] D. Özyürek, M. Yildirim, I. Çiftçi, The tribological properties of A356-SiCpmetalmatrix composites fabricated by thixomoulding technique, Science and Engineering of Composite Materials, 19 (4) (2012) 351–356. https://doi.org/10.1515/secm-2012-0012.

[42] Y.X. Qiao, S.L. Sheng, L.M. Zhang, J. Chen, L.L. Yang, H.L. Zhou, Y.X. Wang, H.B. Li, Z.B. Zheng, Friction and wear behaviors of a high nitrogen austenitic stainless steel Fe-19Cr-15Mn-0.66N, Journal of Mining and Metallurgy, Section B: Metallurgy, 57 (2) (2021) 285–293. https://doi.org/10.2298/JMMB201026025Q.

[43] K.G. Thirugnanasambantham, S. Natarajan, Mechanistic studies on degradation in sliding wear behavior of IN718 and Hastelloy X superalloys at 500 °c, Tribology International, 101 (2016) 324–330. https://doi.org/10.1016/j.triboint.2016.04.016.

[44] C.N. Panagopoulos, K.I. Giannakopoulos, V. Saltas, Wear behavior of nickel superalloy, CMSX-186, Materials Letters, 57 (29) (2003) 4611–4616. https://doi.org/10.1016/S0167-577X(03)00370-7.

[45] G.R. Raghav, A.N. Balaji, N. Selvakumar, D. Muthukrishnan, E. Sajith, Effect of tungsten reinforcement on mechanical, tribological and corrosion behaviour of mechanically alloyed Co-25C Cermet nanocomposites, Materials Research Express, 6 (11) (2018) 0–23. https://doi.org/https://doi.org/10.1088/2053-1591/ab4f0a.

[46] E. Raghav, G.R., Balaji, A.N., Muthukrishnan, D., Sruthi, V., Sajith, An Experimental Investigation on Wear and Corrosion Characteristics of Mg-Co nanocomposites, Materials Research Express, 5 (6) (2018) 0–24. https://doi.org/https://doi.org/10.1088/2053-1591/aac862.

[47] S.M. Banijamali, Y. Palizdar, S. Najafi, A. Sheikhani, M. Soltan Ali Nezhad, P. Valizadeh Moghaddam, H. Torkamani, Effect of Ce Addition on the Tribological Behavior of ZK60 Mg-Alloy, Metals and Materials International, 27 (8) (2021) 2732–2742. https://doi.org/10.1007/s12540-020-00832-4.

[48] M.H. Ghassemi, V. Abouei, M. Moshtaghi, M.T. Noghani, The effect of removing worn particles by ultrasonic cleaning on the wear characterization of LM13 alloy, Surface Engineering and Applied Electrochemistry, 51 (4) (2015) 382–388. https://doi.org/10.3103/S1068375515040067.

[49] G.R. Raghav, S. Janardhanan, E. Sajith, V. Chandran, V. Sruthi, Mechanical and tribological performance of Al-Fe-SiC-Zr hybrid composites produced through powder metallurgy process, Materials Research

Express, 8 (1) 1-13 (2021). https://doi.org/https://doi.org/10.1088/2053-1591/abdb52.

[50] A. Amanov, Improvement in mechanical properties and fretting wear of Inconel 718 superalloy by ultrasonic nanocrystal surface modification, Wear, 446–447 (2020) 203208. https://doi.org/10.1016/j.wear.2020.203208.

[51] Y.H. Lee, I.S. Kim, S.S. Kang, H.D. Chung, A study on wear coefficients and mechanisms of steam generator tube materials, Wear, 250 (1-12) (2001) 718–725. https://doi.org/10.1016/S0043-1648(01)00680-9.

UTICAJ KOLIČINE Y_2O_3 DODATOG LEGURI MA6000 KOJA JE PROIZVEDENA POMOĆU METODE MEHANIČKOG LEGIRANJA NA HABANJE

Ş. Çelik, D. Özyürek*, T. Tunçay

Univerzitet u Karabuku, Tehnološki fakultet, Odsek za proizvodno inženjerstvo, Karabuk, Turska

Apstrakt

U ovom radu je prikazano istraživanje karakteristika legure MA6000 (Ni-Cr-Al) sa dodatkom Y_2O_3 dobijene postupkom mehaničkog legiranja prilikom habanja. Sinterovana superlegura MA6000-X% Y_2O_3 je analizirana putem SEM, EDS i XRD analize, kao i merenjem gustine i tvrdoće. Ispitivanje otpornosti na habanje ove legure je sprovedeno u uređaju za ispitivanje otpornosti na habanje. Tokom ispitivanja brzina klizanja je iznosila 1 ms^{-1} i testovi su se vršili na sobnoj temperaturi. Testovi su izvedeni sa pet različitih rastojanja (200 – 1000 m) i tri različita opterećenja (5 N, 10 N i 15 N). Kao rezultat istraživanja, utvrđeno je da su prahovi superlegure MA6000 sa dodatkom MA homogeni i ljuspičastog oblika. Sa povećanjem količine Y_2O_3, tvrdoća ove superlegure se povećala sa 267 na 431 Hv, ali gustina je blago opala. U svim kompozicijama su primećene različite intermetalne/karbonske faze, kao što su Ni_3Al i MoC. Testovi habanja su pokazali da su gubitak težine i stopa habanja smanjeni, a da je koeficijent trenja (μ) povećan kada se povećala količina dodatog Y_2O_3. Osim toga, utvrđeno je i da se povećanjem primenjenog opterećenja tokom testa habanja povećao gubitak težine, ali da su se stopa habanja i koeficijent trenja (μ) smanjili.

Ključne reči: *Legura dobijena mehaničkim legiranjem; Superlegura; MA6000; Habanje; Y_2O_3*